

HELMOD IN THE WORKS: FROM DIRECT OBSERVATIONS TO THE LOCAL INTERSTELLAR SPECTRUM OF COSMIC-RAY ELECTRONS

M. J. BOSCHINI^{1,2}, S. DELLA TORRE¹, M. GERVASI^{1,3}, D. GRANDI¹, G. JÓHANNESON^{4,5}, G. LA VACCA¹, N. MASI⁶, I. V. MOSKALENKO^{7,8}, S. PENSOTTI^{1,3}, T. A. PORTER^{7,8}, L. QUADRANI^{6,9}, P. G. RANCOITA¹, D. ROZZA^{1,3}, AND M. TACCONI^{1,3}

Draft: January 15, 2018

ABSTRACT

The local interstellar spectrum (LIS) of cosmic-ray (CR) electrons for the energy range 1 MeV to 1 TeV is derived using the most recent experimental results combined with the state-of-the-art models for CR propagation in the Galaxy and in the heliosphere. Two propagation packages, GALPROP and HELMOD, are combined to provide a single framework that is run to reproduce direct measurements of CR species at different modulation levels, and at both polarities of the solar magnetic field. An iterative maximum-likelihood method is developed that uses GALPROP-predicted LIS as input to HELMOD, which provides the modulated spectra for specific time periods of the selected experiments for model-data comparison. The optimized HelMod parameters are then used to adjust GALPROP parameters to predict a refined LIS with the procedure repeated subject to a convergence criterion. The parameter optimization uses an extensive data set of proton spectra from 1997–2015. The proposed CR electron LIS accommodates both the low-energy interstellar spectra measured by Voyager 1 as well as the high-energy observations by PAMELA and AMS-02 that are made deep in the heliosphere; it also accounts for Ulysses counting rate features measured out of the ecliptic plane. The interstellar and heliospheric propagation parameters derived in this study agree well with our earlier results for CR protons, helium nuclei, and anti-protons propagation and LIS obtained in the same framework.

Keywords: cosmic rays — diffusion — elementary particles — interplanetary medium — ISM: general — solar system: general

1. INTRODUCTION

Electrons in the cosmic radiation were identified for the first time about fifty years after the discovery of CRs (Meyer & Vogt 1961; Earl 1961). Subsequently, the origin of the observed spectrum of CR electrons has been one of the most important questions in CR physics. Early CR electron measurements of increasing precision and expanding energy range were made over a series of balloon flights by different experiments (e.g., Fanelow et al. 1969; Buffington et al. 1975; Hartman & Pellerin 1976; Golden et al. 1984, 1994; Basini et al. 1995; Barwick et al. 1998; Boezio et al. 2000; Torii et al. 2001; Grimani et al. 2002). However, the experimental scatter was large because the CR electron spectrum is steeply falling with increasing energy, and the background of heavier CR species is high.

The first high-statistics measurements of the all-electron CR spectrum over a wide energy range were made by the *Fermi* Large Area Telescope (*Fermi*–LAT) launched in 2008 (Atwood et al. 2009). These measurements showed that the all-electron spectrum is flatter than expected with an index about -3 over the energy range 7–1000 GeV (Abdo et al. 2009; Ackermann et al. 2010). PAMELA data (1–625 GeV, Adriani et al. 2011) generally confirmed the *Fermi*–LAT re-

sults albeit with larger error bars, as did the higher precision data from AMS-02 (0.5–1000 GeV, Aguilar et al. 2014a). Even though the precise AMS-02 data showed deviations from the earlier *Fermi*–LAT measurements that are significant due to high statistics and consequently very small error bars, the absolute difference is only $\sim 10\%$ above 20 GeV vs. a factor of ~ 3 –4 in the pre-*Fermi* era. Note that the latest *Fermi*–LAT all-electron spectrum (7–2000 GeV) obtained using a revised event reconstruction and background rejection analysis (Abdollahi et al. 2017) agrees well with AMS-02 results. Above ~ 1 TeV, the all-electron spectrum falls rapidly (H.E.S.S., Aharonian et al. 2008, 2009). The first ever measurement of the all-electron spectrum for energies $\lesssim 100$ MeV outside of the heliosphere has been made by Voyager 1 that reached the heliopause in 2012 (Stone et al. 2013; Cummings et al. 2016).

The strong interest in the CR electron spectrum during the last decade is also fueled by the PAMELA discovery of a continuous rise of the positron fraction up to ~ 100 GeV (Adriani et al. 2009), and expectations of spectral features at very-high energies associated with local CR accelerators (e.g., Kobayashi et al. 2004). The latter are yet to be found, although the dedicated experiment CALET has been operating on the International Space Station (ISS) since August 19, 2015 (Asaoka et al. 2017), and the ISS-CREAM, which was launched to the ISS on August 14, 2017, is also deployed there to make CR measurements in the multi-TeV range (Seo et al. 2014).

The discovery of the rise of the positron fraction by PAMELA, contrary to the expectations based on the pure secondary production of positrons in energetic CR interactions with the interstellar gas (Protheroe 1982; Moskalenko & Strong 1998), was the first clear evidence of new phenomena detected in CRs, even though the first hints of it appeared

¹ INFN, Milano-Bicocca, Milano, Italy

² also CINECA, Segrate, Milano, Italy

³ also Physics Department, University of Milano-Bicocca, Milano, Italy

⁴ Science Institute, University of Iceland, Dunhaga 3, IS-107 Reykjavik, Iceland

⁵ also NORDITA, Roslagstullsbacken 23, 106 91 Stockholm, Sweden

⁶ INFN, Bologna, Italy

⁷ Hansen Experimental Physics Laboratory, Stanford University, Stanford, CA 94305

⁸ Kavli Institute for Particle Astrophysics and Cosmology, Stanford University, Stanford, CA 94305

⁹ also, Physics Department, University of Bologna, Bologna, Italy

in data collected by earlier experiments. The TS93 apparatus launched on a balloon from Fort Sumner, NM, in 1993 measured a flat positron fraction 0.078 ± 0.016 in the range $\sim 5\text{--}60$ GeV (Golden et al. 1996). Subsequent balloon-borne flights by CAPRICE94 in 1994 (Boezio et al. 2000), the HEAT- e^\pm instrument in 1994 and 1995 (Barwick et al. 1997), and HEAT-pbar instrument in 2000 (Beatty et al. 2004), indicated that the positron flux did not fall-off as quickly as expected. However, the experimental error bars in these early experiments were too large to provide convincing evidence for a new phenomenon.

Following the PAMELA discovery the rise of the positron fraction up to 200 GeV was confirmed by the *Fermi*-LAT (Ackermann et al. 2012a), where the geomagnetic field (the ‘‘East-West effect’’) was used to provide the charge sign separation, and then up to ~ 500 GeV with higher precision by AMS-02 (Accardo et al. 2014; Aguilar et al. 2014a). These measurements stimulated an extensive discussion of the origin of the rising positron fraction with dozens of different hypotheses proposed in the literature. They range from conventional astrophysics to non-standard model physics involving various types of dark matter particles. A component with similar origin could be also present in the electron spectrum (e.g., Della Torre et al. 2015).

High-precision measurements of both electrons and positrons over a wide energy range are thus of critical importance toward unveiling the origin of the excess positrons. Meanwhile, the e^\pm spectra and the positron fraction below ~ 10 GeV was found to depend on the solar activity (PAMELA, Adriani et al. 2016). The determination of the true electron LIS is, therefore, of considerable interest for the astrophysics and particle physics communities. In the present paper, the same method – including the treatment of errors – is employed as for the recently published studies devoted to the LIS of CR protons, helium nuclei, and anti-protons (Boschini et al. 2017a).

2. GALPROP AND HELMOD CODES

In this paper, we use a recently developed version of the HELMOD¹⁰ 2D Monte Carlo code for heliospheric CR propagation (Bobik et al. 2012, 2013; Boschini et al. 2017b) combined with the GALPROP¹¹ code for interstellar CR propagation (Jóhannesson et al. 2016; Porter et al. 2017) to take advantage of the progress made in the recent CR electron measurements and to derive a self-consistent electron LIS. The HELMOD code includes all relevant effects and, thus, a full description of the diffusion tensor. HELMOD enables accurate calculations for the heliospheric modulation effect over arbitrary epochs and is easily interfaced with GALPROP.

2.1. Galactic CR propagation with the GALPROP code

The GALPROP code has been under development since the mid-90s (Moskalenko & Strong 1998; Strong & Moskalenko 1998) and is the *de facto* standard code for calculating the propagation of CRs and their associated interstellar emissions. It solves the CR transport equation for a

given source distribution and boundary conditions for all CR species. GALPROP includes all relevant transport and energy loss/gain processes, such as a galactic wind (advection), diffusive reacceleration in the ISM, energy losses, nuclear fragmentation, radioactive decay, and the production of secondary particles and isotopes. The numerical solution of the transport equation can be obtained using different solvers, including a Crank-Nicholson implicit second-order scheme as well as an explicit method. The spatial boundary conditions assume free particle escape. For a given halo size the diffusion coefficient as a function of momentum is determined by fitting model parameters to CR nuclei secondary-to-primary ratios.

The GALPROP code computes a full network of CR primary, secondary and tertiary species from input source abundances. Starting with the heaviest primary nucleus typically considered (^{64}Ni , $A = 64$) the propagation solution is used to compute the source term for its spallation products $A - 1$, $A - 2$, and so forth. These are propagated in turn, and so on down in mass to protons, secondary e^\pm , and \bar{p} . The inelastically scattered p and \bar{p} are treated as separate components (secondary p , tertiary \bar{p}). GALPROP includes a description for the processes of K-capture, electron capture by bare CR nuclei and stripping, as well as knock-on electrons. More details are given in Ptuskin et al. (2006), Strong et al. (2007), Vladimirov et al. (2011), and Jóhannesson et al. (2016), as well as the description of the most recent version of GALPROP (v. 56) – see Moskalenko et al. (2017) and Porter et al. (2017), and references therein.

2.2. HELMOD code for heliospheric CR transport

GALPROP provides the predictions for the LIS of all CR species. However, they cannot be compared to the direct CR measurements made at Earth’s orbit, or generally in the inner heliosphere, because of the effect of the so-called heliospheric or solar modulation. This modulation is the combined effect of the expanding magnetic fields and the solar wind (SW) whose properties depend on the level of solar activity (e.g., see Boschini et al. 2017a,b).

The propagation of CRs in the heliosphere was first studied by Parker (1965), who formulated the transport equation (also called the Parker equation – see, e.g., the discussion in Bobik et al. 2012, and reference therein):

$$\frac{\partial U}{\partial t} = \frac{\partial}{\partial x_i} \left(K_{ij}^S \frac{\partial U}{\partial x_j} \right) + \frac{1}{3} \frac{\partial V_{sw,i}}{\partial x_i} \frac{\partial}{\partial T} (\alpha_{rel} TU) - \frac{\partial}{\partial x_i} [(V_{sw,i} + v_{d,i})U], \quad (1)$$

where U is the number density of Galactic CR particles per unit of kinetic energy T (GeV/nucleon), t is time, $V_{sw,i}$ is the SW velocity along the axis x_i , K_{ij}^S is the symmetric part of the diffusion tensor, $v_{d,i}$ is the particle magnetic drift velocity (related to the anti-symmetric part of the diffusion tensor), and $\alpha_{rel} = \frac{T+2m_r c^2}{T+m_r c^2}$, with m_r – the particle rest mass per nucleon in units of GeV/nucleon. The terms in the Parker equation describe: (i) the *diffusion* of Galactic CRs scattered by magnetic turbulences, (ii) the *adiabatic* energy losses/gains due to the propagation in the expanding magnetic fields carried in the SW, (iii) an *effective convection* resulting from the SW convection with velocity \vec{V}_{sw} , and (iv) the *drift effects* related to the drift velocity (\vec{v}_{drift}). Overall, the heliospheric modula-

¹⁰ In this work we use HELMOD version 3.5, available from <http://www.helmod.org/>. The origin of the HELMOD code goes back to the work by Gervasi, Rancoita, Usoskin, & Kovaltsov (1998) (see, for instance, Bobik et al. 2003, 2009; Bobik et al. 2012; Della Torre et al. 2012; Bobik et al. 2013, 2016; Boschini et al. 2017b). It has been under continuous development since that time.

¹¹ <http://galprop.stanford.edu>

tion results in energy losses and suppression of the fluxes of CR species compared to the LIS that are energy- and charge-sign-dependent. These effects are controlled by the polarity of the solar magnetic field and by the level of solar activity.

The particle transport within the heliosphere, from the Termination Shock (TS) to Earth's orbit, is treated in this paper using the HELMOD code. HELMOD integrates the Parker (1965) transport equation using a Monte Carlo approach involving stochastic differential equations; for further details of the method and code see Bobik et al. (2012, 2016).

In previous models of CR propagation in the heliosphere, the parallel diffusion coefficient (K_{\parallel}) was assumed to have a sharp break at ~ 1 GV, in the transitional region between the two regimes at high and low rigidities (e.g., see Perko 1987; Alanko-Huotari et al. 2007; Strauss et al. 2011; Bobik et al. 2012). However, as the accuracy of the collected data increased, it becomes clear that a smooth transition between the two regimes is necessary. The functional form of such a transition that is currently employed in HELMOD (see Equation 5 in Boschini et al. 2017b) is consistent with those presented in Burger & Hattigh (1998) for the same rigidity interval.

The normalization of the parallel component K_{\parallel} of the symmetric part of the diffusion tensor K_{ij}^S is determined by the so-called diffusion parameter K_0 , as defined by Eq. (2) of Boschini et al. (2017b, and references therein). In turn, the diffusion parameter K_0 includes a correction factor that rescales the absolute value proportionally to the drift contribution. This correction factor is evaluated in Boschini et al. (2017a) using the proton spectrum during the period of positive polarity of the heliospheric magnetic field (HMF), and accounts for the presence of the latitudinal structure in the spatial distribution of Galactic CRs. The same correction factor is now applied to electron propagation ($q < 0$) during the negative HMF polarity period¹² ($A < 0$), so that an equivalent scaling¹³ is applied to periods with $qA > 0$.

The drift treatment in HELMOD follows the formalism originally developed by Potgieter & Moraal (1985) and refined using Parker's magnetic field with polar correction described in Bobik et al. (2013). During high activity periods the heliospheric magnetic field is far from being considered regular, therefore, we introduced a correction factor suppressing any drift velocity at solar maximum.

As discussed by Boschini et al. (2017b), the validity of the HELMOD code is verified down to about 1 GV rigidities (equivalent to ~ 1 GeV in kinetic energy for electrons). Lower rigidities/energies are not considered in the present work because to do so requires additional refinement for the description of the solar modulation in the outer heliosphere – between TS and interstellar space (see, e.g., Scherer et al. 2011; Dialynas et al. 2017) – as well as inclusion of the turbulence in the calculation of the drift coefficient (see, e.g., Engelbrecht et al. 2017). However, Voyager 1 electron data is used as a guideline.

¹² A similar correction has to be evaluated for the negative-charge particle diffusion during the positive HMF polarity period ($qA < 0$). The negative-charge particles are subject to a correction that is opposite to the one applied to the positive-charge particles.

¹³ HELMOD Parameters – usually determined at 1 AU – are used for the properties of any heliospheric sector, according to the time required by the solar wind coming from the Sun to reach such a region (Bobik et al. 2012; Boschini et al. 2017b). When this is not accounted for there is an effective time delay in the correlation between time variations of the parameters of the solar magnetic field, as measured at Earth, and the observed intensity variations of GCRs (see, e.g., Tomassetti et al. 2017, and references therein).

Table 1
Best-fit propagation parameters for electrons

N	Parameter	Best Value
1	z_h , kpc	4.0
2	D_0 , 10^{28} cm ² s ⁻¹	4.3
3	δ	0.405
4	V_{Alf} , km s ⁻¹	31
5	dV_{conv}/dz , km s ⁻¹ kpc ⁻¹	9.8

Table 2
Electron injection spectrum

Parameters	Values
R_0	190 MV
R_1	6 GV
R_2	95 GV
γ_0	2.57
γ_1	1.40
γ_2	2.80
γ_3	2.40/2.54 ^a

^a If an additional component to the electron spectrum is added, see a discussion in Section 4.

3. INTERSTELLAR PROPAGATION

The tuning procedure employed in this paper is the same that was used by Boschini et al. (2017a). A short description of the method is provided below.

The Markov Chain Monte Carlo (MCMC) interface to v.56 of GALPROP was adapted from CosRayMC (Liu et al. 2012) and, in general, from the COSMOMC package (Lewis & Bridle 2002). An iterative procedure was developed that calculates LIS with GALPROP, passing the results to HELMOD to produce the modulated spectra for specific time periods for comparison with AMS-02 data, which are the observational constraints. The goodness estimator of the parameter scan is the natural logarithm of the likelihood. For computational convenience this is built using χ^2 from all observables: hundreds of thousands of samples were generated and the Log-Likelihood used to accept or reject each sample. The scan is terminated when the Log-Likelihood is maximized.

The basic features of CR propagation in the Galaxy are well-known, but the exact values of propagation parameters depend on the assumed propagation model and accuracy of selected CR data. Therefore, the MCMC procedure is used to determine the propagation parameters employing the best available CR measurements. The five propagation parameters that have the largest effect on the overall shape of CR spectra were left free in the scan that used a 2D GALPROP model: the Galactic halo half-width z_h , the normalization of the diffusion coefficient D_0 and the index of its rigidity dependence δ , the Alfvén velocity V_{Alf} , and the gradient of the convection velocity dV_{conv}/dz ($V_{\text{conv}} = 0$ in the plane, $z = 0$). The spatial distribution of CRs near the Sun depends only weakly on the chosen radial size of the Galaxy if its distance is farther than the halo size (e.g., Ackermann et al. 2012b). The radial boundary is therefore set to 20 kpc.

The best values for the main propagation parameters tuned to the AMS-02 data are listed in Table 1. The values are similar to those obtained by Boschini et al. (2017a), within the quoted error bands, while the convection velocity V_{conv}

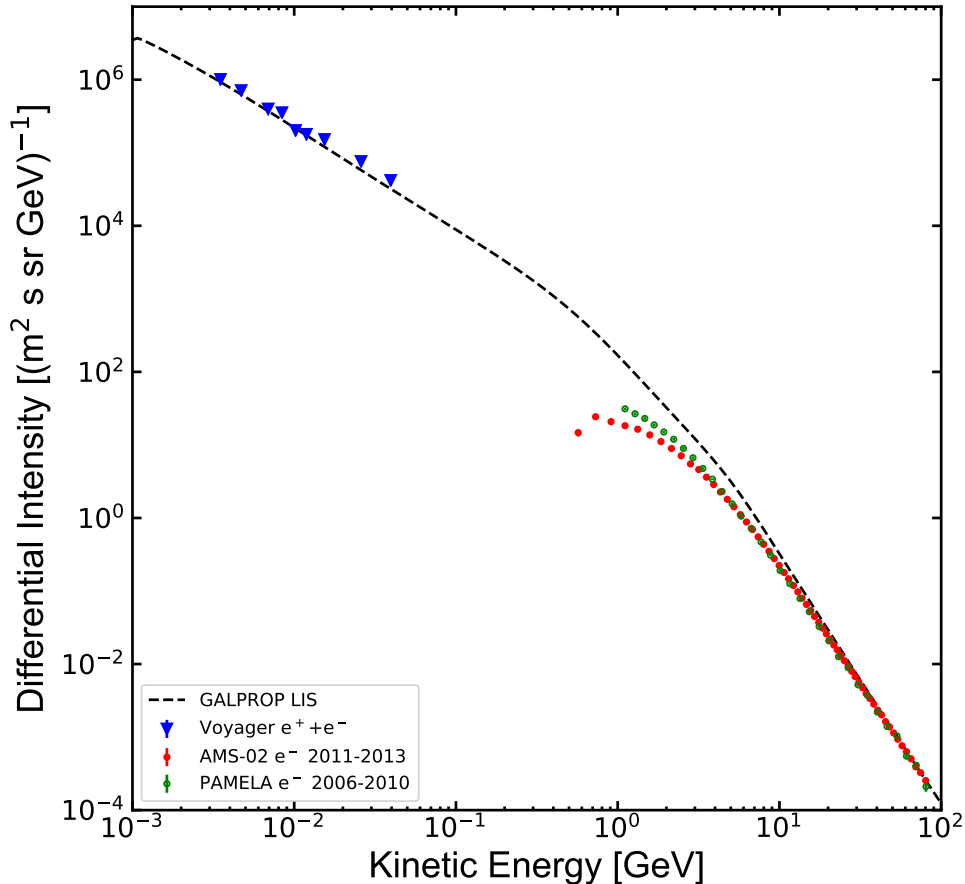


Figure 1. The electron LIS (dashed) as derived from the MCMC procedure compared with AMS-02, PAMELA and Voyager 1 measurements (see text).

is set to 0 in the plane. For example, to get a more consistent electron LIS, the Alfvén velocity V_{Alf} was increased by $\sim 2 \text{ km s}^{-1}$. As already discussed by Boschini et al. (2017a), simultaneous inclusion of both reacceleration and convection is needed to describe the high precision AMS-02 data, particularly in the range below 20 GV where the modulation effects on CR spectra are significant. For more details the reader is referred to the above-mentioned paper.

The MCMC procedure is used only for first step to define a consistent set for the Galactic CR propagation parameters. The HELMOD module was then used for a methodical calibration of the LIS spectral parameters. Parameters of the injection spectra, such as spectral indices γ_i and the break rigidities R_i , were left free, but their exact values depend on the solar modulation, so the low-energy parts of the spectra are tuned together with the solar modulation parameters as described below.

To refine the LIS description smoothing features to the breaks in the injection spectrum were added. Reproducing the electron spectrum from MeV to TeV energies requires an injection spectrum with three spectral breaks. MCMC scans in γ_i and R_i were performed using CR electron measurements by AMS-02 (Aguilar et al. 2014b) and by Voyager 1 (Cummings et al. 2016) as constraints. At the next step, these parameters were slightly modified together with the solar modulation parameters in order to find the best-fit solution for the electron LIS, as explained by Boschini et al. (2017a). Reproduction of the low-energy electron LIS measurements by Voy-

ager 1 requires a break around $R_0 \sim 190 \text{ MV}$. The resulting best-fit spectral parameters are shown in Table 2.

Note that the only data available to tune the electron LIS below AMS-02 energies are coming from Voyager 1. Unfortunately, the Electron Telescope (TET) aboard the Voyager 1 spacecraft cannot discriminate between electrons and positrons, so it provides only the all-electron spectrum. On the other hand, GALPROP calculations indicate that the secondary positron fraction decreases as energy decreases being $\lesssim 35\%$ at its maximum contribution for $\sim 200 \text{ MeV}$ energies, and becomes as small as a few per cent or less below $\sim 20 \text{ MeV}$ (e.g., Porter et al. 2008). Therefore, assuming that only electrons are present in CRs at low energies the maximum error in the results at these energies would be $\sim 30\%$.

3.1. Electron LIS at low and Intermediate energies

Since the end of August, 2012, the Voyager 1 mission is exploring interstellar space providing invaluable data on the composition of Galactic CRs at low energies (Stone et al. 2013; Cummings et al. 2016). In the current analysis Voyager 1 data (Cummings et al. 2016) taken between December 2012 and June 2015 is used as a constraint for evaluating the electron LIS, as described above. A comparison of the Voyager 1 all-electron spectrum in the kinetic energy range 3–74 MeV and the proposed model for the LIS is shown in Figure 1. The combined model provides a good description of the electron LIS at low energies.

At high energies, where the CR fluxes are not affected by

Table 3
Normalization corrections applied to the electron LIS

Dataset group	Experiment	Time span	Normalization correction	Reference
a)	PAMELA	5 years integrated spectrum	0.81	Adriani et al. (2011)
b)	PAMELA	6 months integrated spectrum	0.9	Adriani et al. (2015)
c)	AMS-02	3 years integrated spectrum	1.0	Aguilar et al. (2014b)

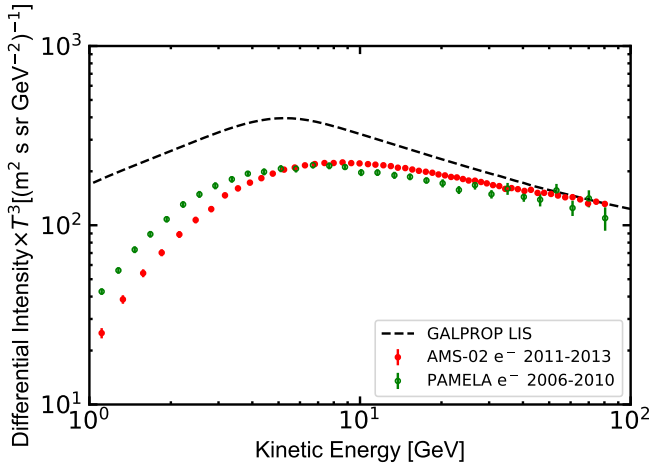


Figure 2. The proposed electron LIS is compared with high-energy all-electron data from AMS-02 and PAMELA experiments.

the heliospheric modulation, the most recent measurements by AMS-02 and PAMELA up to 90 GeV are included and shown in Figure 2. The electron LIS at even higher energies is discussed in Sect. 4.

It can be seen that even though the AMS-02 (Aguilar et al. 2014b) and PAMELA data (Adriani et al. 2011) in Figure 2 are consistent within the error bars, the systematic difference between the datasets can be as large as $\sim 20\%$ in the energy range 30–90 GeV. Speculation on the possible origin(s) of this difference is not made here. However, it is clear that it is not the effect of solar modulation because it should be insignificant at these energies. For the MCMC procedure (Sect. 2.1) the AMS-02 data is used because it has the smallest error bars.

3.2. Data at Earth and outside of the ecliptic plane

This section illustrates an application of the HELMOD code to derivation of the modulated electron spectra at Earth. The spectra have to be compared to those measured by AMS-02 and PAMELA during periods of low (i.e., PAMELA from 2006 to 2010, Adriani et al. 2011, 2015) and high solar activity (i.e., AMS-02 from 2011 to 2013, Aguilar et al. 2014b). The available data are integrated over a period of a few months to years. To reproduce the conditions of both low and high solar activity, the HELMOD modulated spectra are evaluated for each Carrington Rotation within the period appropriate to the corresponding dataset. The obtained results are then used to evaluate a unique normalized probability function for the modulation tool described in Section 3.1 of Boschini et al. (2017a).

Improvements in the data analysis procedure and in the simulation of the time dependence of the tracking system performance of PAMELA (Adriani et al. 2015) lead to a $\sim 10\%$ increase in the overall normalization of the CR electron fluxes measured in the period from July, 2006 – December, 2009 compared to earlier results (Adriani et al. 2011). However,

it is not enough to account for a systematic discrepancy of $\sim 20\%$ between AMS-02 and earlier results from PAMELA (Adriani et al. 2011). Due to the smaller quoted systematic uncertainties, the AMS-02 data are used as the reference. In this work a normalization factor for the electron LIS that is listed in Table 3 is calculated for each presented dataset.

The computed modulated spectra, for both low and high solar activity periods, are shown in Figures 3 and 4. The details of the modulation model are described in Sect. 2.2 and applied to the LIS described in Sect. 3.1. The high energy part of the spectrum is not affected by the solar modulation, and, therefore, is not discussed here. Simulated spectra are in a good agreement with experimental data in the energy range from 1 GeV to 90 GeV. The $\sim 2\sigma$ deviations seen in the energy range $\lesssim 3$ GeV are present in all spectra, and this most likely implies that the injection spectrum needs some additional adjustments. Further comparison with the data is made in Appendix A that also includes data taken by PAMELA around solar minimum (Adriani et al. 2015).

A reliable model for heliospheric modulation requires a proper modeling of CR distribution in the whole heliospheric volume, including space outside the ecliptic plane and at large distances from the Sun. Since 1990s and until 2009, the Ulysses spacecraft (see e.g. Sanderson et al. 1995; Marsden 2001; Balogh et al. 2001) explored the heliosphere outside the ecliptic plane up to $\pm 80^\circ$ in solar latitude and at distances $\sim 1\text{--}5$ AU from the Sun. In particular, observations of particle flux were performed using the Cosmic Ray and Solar Particle Investigation Kiel Electron Telescope (COSPIN/KET) and High Energy Telescope (COSPIN/HET). Figure 6 shows the Ulysses counting rate normalized to the average value. Data for Ulysses were taken from Ulysses Final Archive¹⁴. The analyzed data come from the KET electron channel E300-B (Rastoin et al. 1996, electron energies of 0.9–4.6 GeV) using the Carrington Rotation average.

HELMOD calculations are made for electrons of 0.6–10 GeV for each Carrington Rotation at the same distance and solar latitude as the Ulysses spacecraft. In order to correctly weight the spectral energy distribution, the calculated differential flux is then convolved with the subchannel response function available in Rastoin et al. (1996). The error band was evaluated using the procedure described in Boschini et al. (2017a). Figure 6 shows a comparison of the Ulysses data with the HELMOD calculations. Both experimental data and simulations are normalized to their corresponding mean values to allow a relative comparison along the solar cycle. The model reproduces the general features of the latitudinal gradients observed during the fast scans of 1994–1995 and 2007. Moreover, the agreement is still acceptable along the whole orbit, which extends as far as ~ 3 AU. We note that the purpose of Figure 6 is only to demonstrate the qualitative agreement between the HELMOD calculations and observations. A proper quantitative comparison with the Ulysses data

¹⁴ <http://ufa.esac.esa.int/ufa>

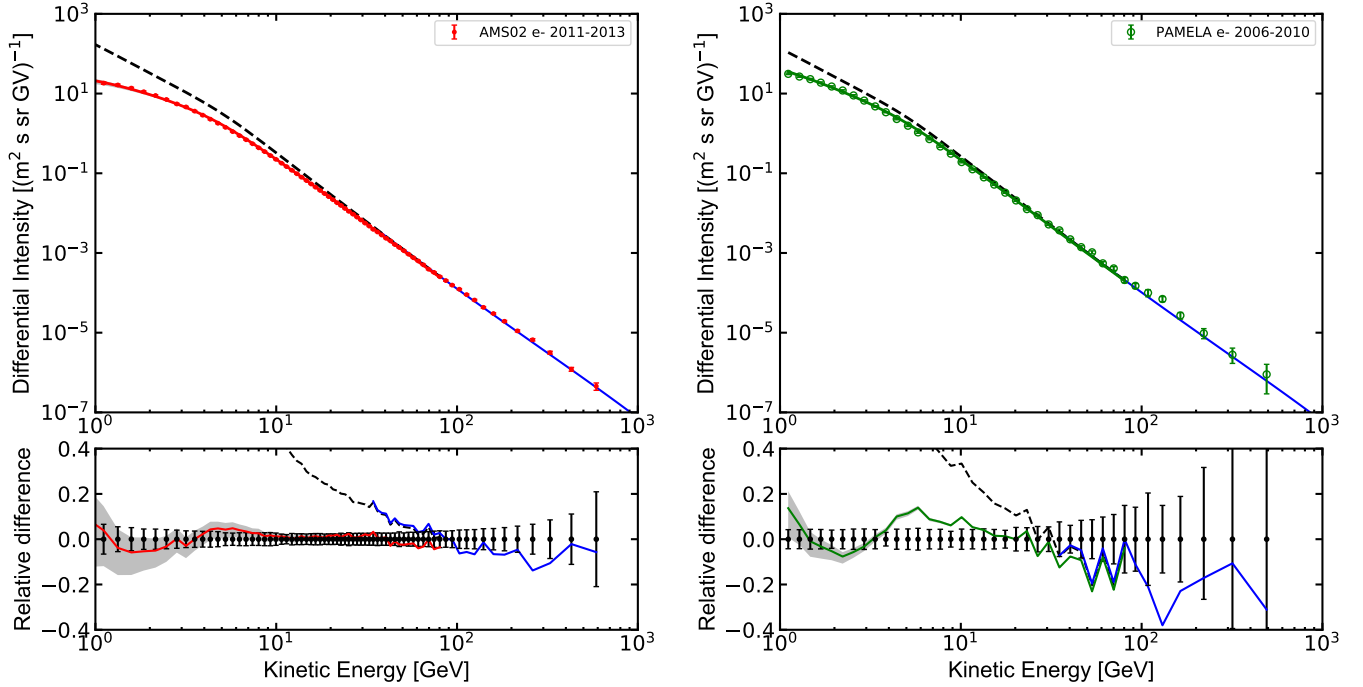


Figure 3. Differential intensity of CR electrons for AMS-02 2011-2013 (left) and PAMELA 2006-2010 (right) datasets. Points represent experimental data, the black dashed line is the GALPROP LIS, and the red/green solid lines are the computed modulated spectra. The blue solid line represents the expected LIS including the high energy electron excess contribution (see text). The bottom panel shows the relative difference between the numerical solutions and the experimental data.

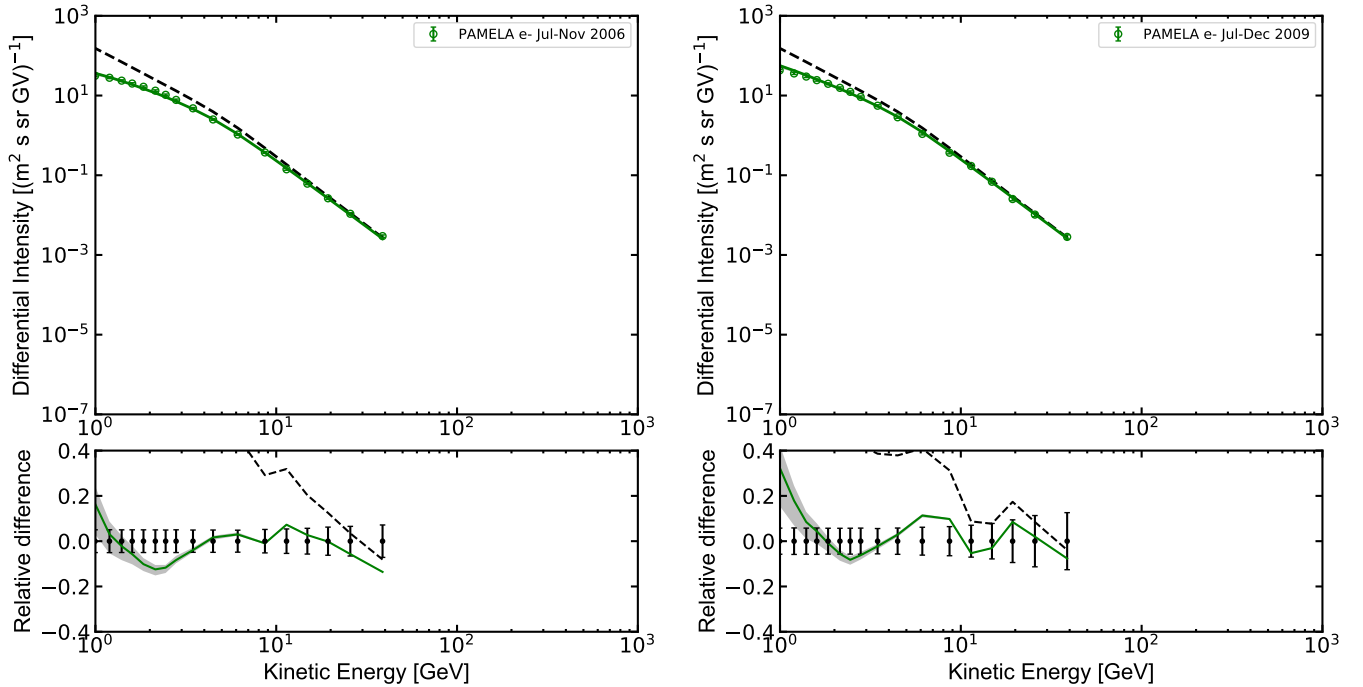


Figure 4. Differential intensity of CR electrons for PAMELA 2006 (left) and PAMELA 2009 (right) datasets. Points represent experimental data, the black dashed line is the GALPROP LIS, and green solid lines are the computed modulated spectra. The bottom panel shows the relative difference between the numerical solution and the experimental data.

would require a calculation that combines several energy bins weighted with the Ulysses response function and detector efficiency.

4. ELECTRON LIS

In addition to the plots and tabulated data presented in Sect. 3.2 and the Appendix, we provide a parameterization $F(T)$ of the GALPROP LIS (Figure 1) from 2 MeV up to 90

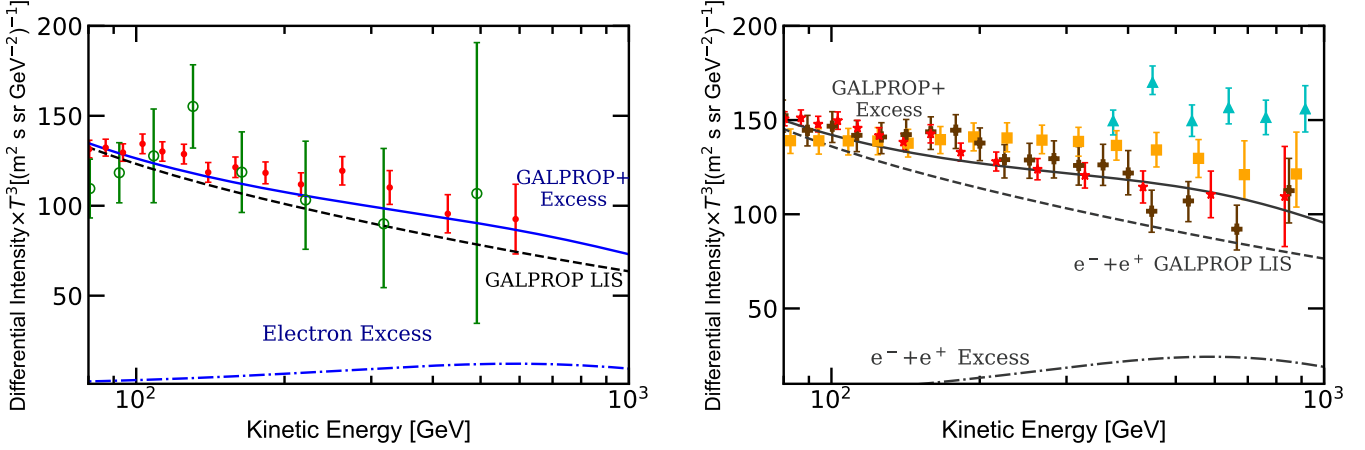


Figure 5. High energy LIS for electrons (left panel) and “all-electrons” (right panel) along with AMS-02 (red points, Aguilar et al. 2014b,a), PAMELA (green open circles, top panel, Adriani et al. 2011), *Fermi*-LAT (orange squares, bottom panel, Ackermann et al. 2012a), CALET (brown crosses, bottom panel, Adriani et al. 2017) and H.E.S.S. (cyan triangles, bottom panel, Aharonian et al. 2008) measurements. The GALPROP LIS is plotted with the dashed line, the estimated high-energy omnidirectional-intensity positron excess is plotted with the dot-dash line (multiplied by a factor of 2 in the bottom panel to account for the identical electron excess, see text) and, finally the sum of GALPROP LIS and electron and positron excess components is plotted with the solid line.

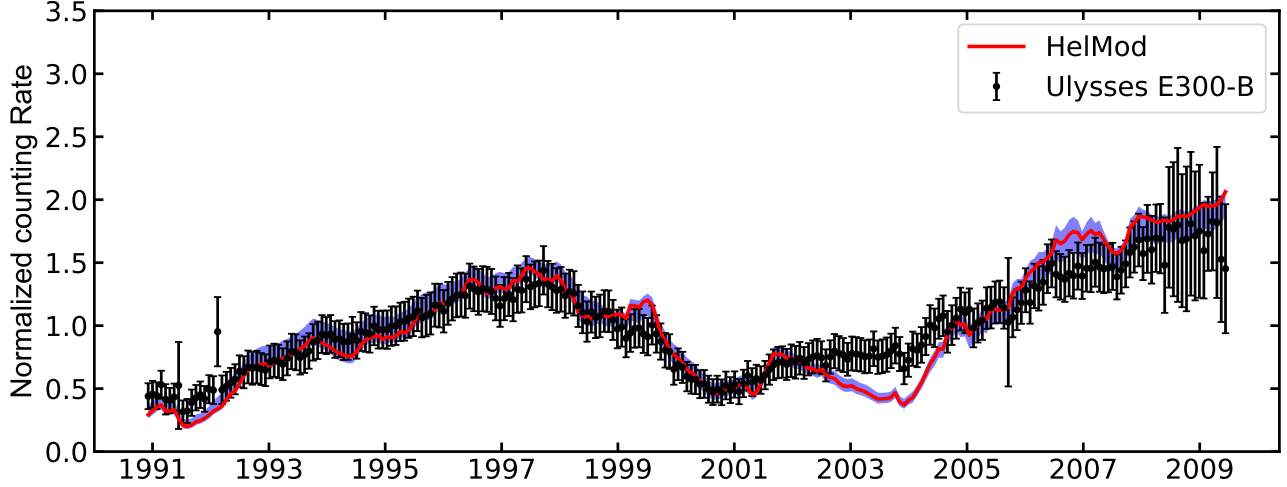


Figure 6. Ulysses counting rate normalized to the average value for the KET electron channel E300-B (electron energies of 0.9–4.6 GeV) as a function of time, where each point is an average over one Carrington rotation. The red solid line is the HELMOD calculation for electrons of 0.6–10 GeV convolved with the subchannel response function for each Carrington rotation at same distance and solar latitude of the Ulysses spacecraft. Blue area shows systematic errors associated with model calculations.

GeV as a function of kinetic energy in GeV:

$$F(T) = \begin{cases} \frac{1.181 \times 10^{11} T^{-12.061}}{1 + 4.307 \times 10^8 T^{-9.269} + 3.125 \times 10^8 T^{-10.697}}, & T < 6.88 \text{ GeV} \\ 995.598 T^{-3.505} + 4.423 T^{-2.620}, & T \geq 6.88 \text{ GeV} \end{cases} \quad (2)$$

where the units are $(\text{m}^2 \text{ s sr GeV})^{-1}$. This fit reproduces the GALPROP electron LIS with an accuracy better than 5% for the whole quoted energy range.

The electron LIS that results from the model calculations is in a good agreement with data (Figure 5). Meanwhile, it may harbor an additional electron component from an unknown source of the same nature as that of the excess positrons (Adriani et al. 2009; Accardo et al. 2014). If charge-sign symmetry is assumed, i.e. that the electron and positron components coming from an unknown source have identical spectra, then the spectral shape of such an additional electron component

can be derived from AMS-02 positron measurements (Aguilar et al. 2014b). The spectrum of an additional component, “the signal,” $S(T)$ can be parametrized as a function of kinetic energy as:

$$S(T) = 4.5 \times 10^{-3} T^{-1.53} e^{-\frac{T}{400 \text{ GeV}}} (\text{m}^2 \text{ s sr GeV})^{-1} \quad (3)$$

This involves a re-tuning of the electron injection spectrum above the break at 95 GV (γ_3 in Table 2). This parameterization also takes into account the standard astrophysical background of secondary positrons evaluated to be $\lesssim 6\%$ at 30 GeV (Moskalenko & Strong 1998; Accardo et al. 2014).

With an addition of the extra components, the electron and all-electron spectra (Aguilar et al. 2014a) match the AMS-02 data well (Figure 5). The calculated all-electron spectrum includes the astrophysical background of positrons ($\lesssim 6\%$ relative to the all-electron LIS) that is also used as an estimate of the systematic uncertainty. The all-electron spectrum includes twice the positron excess that accounts for both extra

electron and positron components. The inclusion of the extra electron and positron components in equal amounts improves the agreement with the AMS-02 data (Della Torre et al. 2015). A possible origin of this excess will be discussed in a forthcoming paper devoted to the positron LIS.

5. CONCLUSIONS

The electron LIS derived in the current work provides a good description of the Voyager 1, PAMELA, and AMS-02 data over the energy range from 1 MeV to 1 TeV. The data for solar cycles 23 and 24 to be successfully reproduced within a single framework. This includes a fully realistic and exhaustive description of the relevant CR physics. Given their high precision, recent AMS-02 electron and positron data can be used to put useful constraints on the origin of the positron excess – to be discussed in the forthcoming paper. This work complements earlier results on the proton, He, and antiproton LIS illustrating a significant potential of the combined GALPROP-HELMOD framework.

Special thanks are made to Pavol Bobik, Giuliano Boella, Karel Kudela, Marian Putis and Mario Zannoni for their support of the HELMOD code and many useful suggestions. This work is supported by ASI (Agenzia Spaziale Italiana) under contract ASI-INFN I/002/13/0 and ESA (European Space Agency) contract 4000116146/16/NL/HK. Igor Moskalenko and Troy Porter acknowledge support from NASA Grant No. NNX17AB48G.

REFERENCES

- Abdo, A. A. et al. 2009, *Phys. Rev. Lett.*, 102, 181101
 Abdollahi, S. et al. 2017, *Phys. Rev. D*, 95, 082007
 Accardo, L. et al. 2014, *Phys. Rev. Lett.*, 113, 121101
 Ackermann, M. et al. 2012a, *Phys. Rev. Lett.*, 108, 011103
 —. 2010, *Phys. Rev. D*, 82, 092004
 —. 2012b, *ApJ*, 750, 3
 Adriani, O. et al. 2017, *Phys. Rev. Lett.*, 119, 181101
 Adriani, O. et al. 2009, *Nature*, 458, 607
 —. 2011, *Phys. Rev. Lett.*, 106, 201101
 —. 2015, *ApJ*, 810, 142
 —. 2016, *Phys. Rev. Lett.*, 116, 241105
 Aguilar, M. et al. 2014a, *Phys. Rev. Lett.*, 113, 221102
 —. 2014b, *Phys. Rev. Lett.*, 113, 121102
 Aharonian, F. et al. 2009, *A&A*, 508, 561
 —. 2008, *Phys. Rev. Lett.*, 101, 261104
 Alanko-Huotari, K., Usoskin, I. G., Mursula, K., & et al. 2007, *J. Geophys. Res.*, 112
 Asaoka, Y. et al. 2017, *Astropart. Phys.*, 91, 1
 Atwood, W. B. et al. 2009, *ApJ*, 697, 1071
 Balogh, A., Marsden, R. G., & Smith, E. J. 2001, The heliosphere near solar minimum. The Ulysses perspective
 Barwick, S. W. et al. 1997, *ApJ*, 482, L191
 —. 1998, *ApJ*, 498, 779
 Basini, G. et al. 1995, 24th Int. Cosmic Ray Conf. (Rome), 3, 1
 Beatty, J. J. et al. 2004, *Phys. Rev. Lett.*, 93, 241102
 Bobik, P. et al. 2013, *Adv. Astron.*, 2013
 —. 2012, *ApJ*, 745, 132
 Bobik, P. et al. 2009, in *Astroparticle, Particle and Space Physics, Detectors and Medical Physics Applications: Volume 5. Proceedings of the 11th Conference*. Villa Olmo, Como, Italy, 5–9 October 2009 (WORLD SCIENTIFIC), 760–764
 —. 2016, *J. Geophys. Res. (Space Phys.)*, 121, 3920
 Bobik, P., Gervasi, M., Grandi, D., Rancoita, P. G., & Usoskin, I. G. 2003, in *Astroparticle, Particle and Space Physics, Detectors and Medical Physics Applications: Volume 2. Proceedings of the 8th Conference Villa Olmo, Como, Italy, 6–11 October 2003* (WORLD SCIENTIFIC), 23–28
 Boezio, M. et al. 2000, *ApJ*, 532, 653
 Boschini, M. J. et al. 2017a, *ApJ*, 840, 115
 Boschini, M. J., Della Torre, S., Gervasi, M., La Vacca, G., & Rancoita, P. G. 2017b, Available online on *Adv. Space Res.*
 doi:10.1016/j.asr.2017.04.017
 Buffington, A., Orth, C. D., & Smoot, G. F. 1975, *ApJ*, 199, 669
 Burger, R. A., & Hattin, M. 1998, *ApJ*, 505, 244
 Cummings, A. C. et al. 2016, *ApJ*, 831, 18
 Della Torre, S. et al. 2012, *Adv. Space Res.*, 49, 1587
 Della Torre, S., Gervasi, M., Rancoita, P. G., & et al. 2015, *J. High Energy Astrophys.*, 8, 27
 Dialynas, K., Krimigis, S. M., Mitchell, D. G., Decker, R. B., & Roelof, E. C. 2017, *Nature Astron.*, 1, 0115
 Earl, J. A. 1961, *Phys. Rev. Lett.*, 6, 125
 Engelbrecht, N. E., Strauss, R. D., le Roux, J. A., & Burger, R. A. 2017, *ApJ*, 841, 107
 Fanselow, J. L., Hartman, R. C., Hildebrand, R. H., & Meyer, P. 1969, *ApJ*, 158, 771
 Gervasi, M., Rancoita, P., Usoskin, I., & Kovaltsov, G. 1998, *Nuclear Physics B Proceedings Supplements*, 6th ICATPP Conf., Como 5-9 Oct 1998, 78, 26
 Golden, R. L. et al. 1994, *ApJ*, 436, 769
 Golden, R. L., Mauger, B. G., Badhwar, G. D., Daniel, R. R., Lacy, J. L., Stephens, S. A., & Zipse, J. E. 1984, *ApJ*, 287, 622
 Golden, R. L. et al. 1996, *ApJ*, 457, L103
 Grimani, C. et al. 2002, *A&A*, 392, 287
 Hartman, R. C., & Pellerin, C. J. 1976, *ApJ*, 204, 927
 Jóhannesson, G. et al. 2016, *ApJ*, 824, 16
 Kobayashi, T., Komori, Y., Yoshida, K., & Nishimura, J. 2004, *ApJ*, 601, 340
 Lewis, A., & Bridle, S. 2002, *Phys. Rev. D*, 66, 103511
 Liu, J., Yuan, Q., Bi, X.-J., Li, H., & Zhang, X. 2012, *Phys. Rev. D*, 85, 043507
 Marsden, R. G. 2001, *The Publications of the Astronomical Society of the Pacific*, 113, 129
 Meyer, P., & Vogt, R. 1961, *Phys. Rev. Lett.*, 6, 193
 Moskalenko, I. V., Jóhannesson, G., Orlando, E., Porter, T. A., & Strong, A. W. 2017, *Proc. 35th Int. Cosmic Ray Conf. (Busan)*, PoS(ICRC2017)279
 Moskalenko, I. V., & Strong, A. W. 1998, *ApJ*, 493, 694
 Parker, E. N. 1965, *Planet. Space Sci.*, 13, 9
 Perko, J. S. 1987, *Å*, 184, 119
 Porter, T. A., Jóhannesson, G., & Moskalenko, I. V. 2017, *ApJ*, 846, 67
 Porter, T. A., Moskalenko, I. V., Strong, A. W., Orlando, E., & Bouchet, L. 2008, *ApJ*, 682, 400
 Potgieter, M. S., & Moraal, H. 1985, *ApJ*, 294, 425
 Protheroe, R. J. 1982, *ApJ*, 254, 391
 Ptuskin, V. S., Moskalenko, I. V., Jones, F. C., Strong, A. W., & Zirakashvili, V. N. 2006, *ApJ*, 642, 902
 Rastoin, C. et al. 1996, *A&A*, 307, 981
 Sanderson, T. R., Marsden, R. G., Wenzel, K.-P., Balogh, A., Forsyth, R. J., & Goldstein, B. E. 1995, *Space Science Reviews*, 72, 291
 Scherer, K., Fichtner, H., Strauss, R. D., Ferreira, S. E. S., Potgieter, M. S., & Fahr, H.-J. 2011, *ApJ*, 735, 128
 Seo, E. S. et al. 2014, *Adv. Spa. Res.*, 53, 1451
 Stone, E. C., Cummings, A. C., McDonald, F. B., Heikkilä, B. C., Lal, N., & Webber, W. R. 2013, *Science*, 341, 150
 Strauss, R. D., Potgieter, M. S., Büsching, I., & Kopp, A. 2011, *ApJ*, 735, 83
 Strong, A. W., & Moskalenko, I. V. 1998, *ApJ*, 509, 212
 Strong, A. W., Moskalenko, I. V., & Ptuskin, V. S. 2007, *Ann. Rev. Nucl. Part. Sci.*, 57, 285
 Tomassetti, N., Orcinha, M., Barao, F., & Bertucci, B. 2017, Submitted to *ApJ*, arXiv: 1707.06916
 Torii, S. et al. 2001, *ApJ*, 559, 973
 Vladimirov, A. E. et al. 2011, *Comp. Phys. Comm.*, 182, 1156

APPENDIX
SUPPLEMENTARY MATERIAL

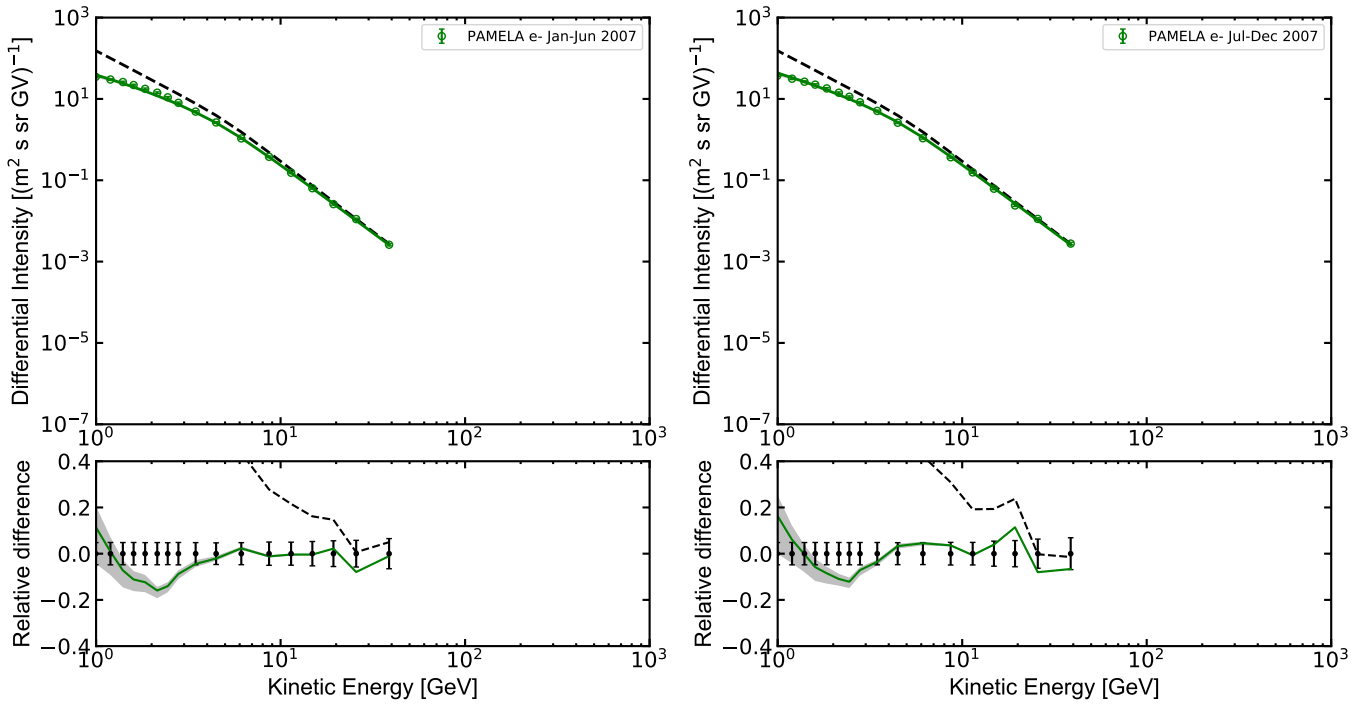


Figure 7. Differential intensity of CR electrons for PAMELA 2007 datasets. Points represent experimental data, the black dashed line is the GALPROP LIS, and the solid lines are the computed modulated spectra. The bottom panel shows the relative difference between the numerical solution and experimental data.

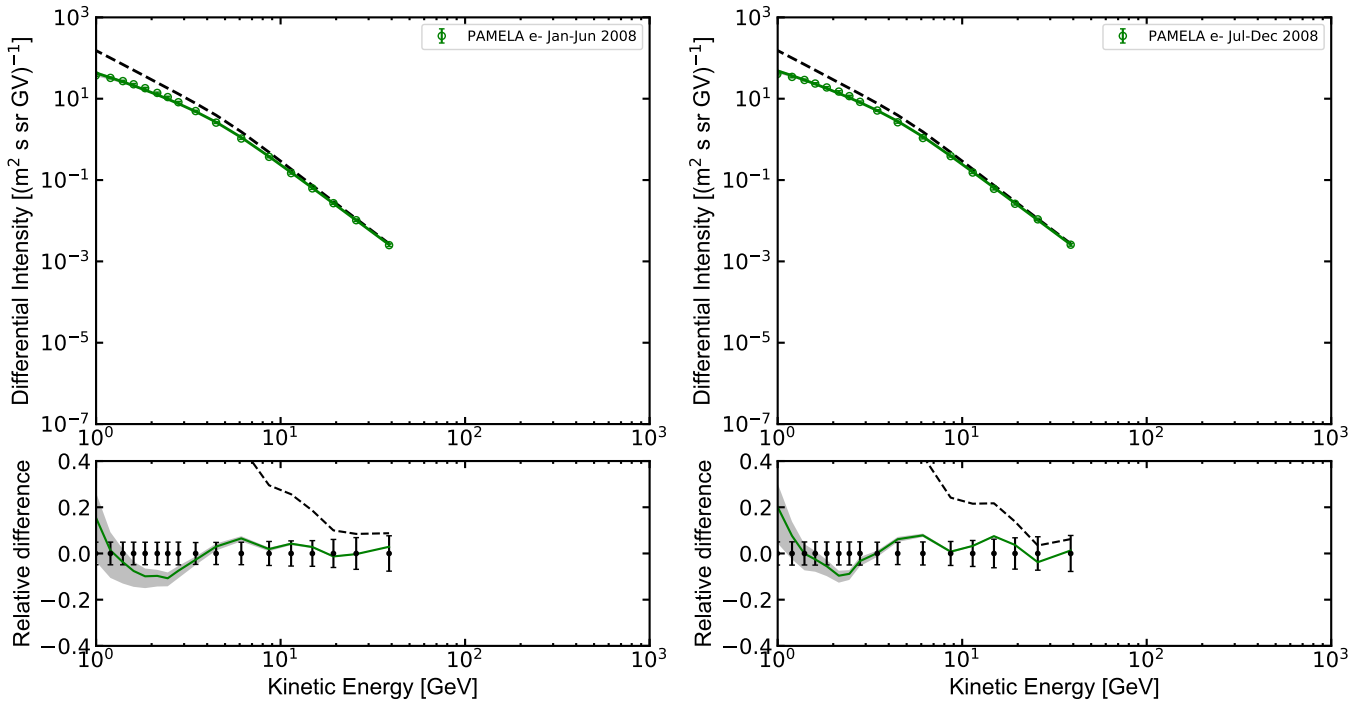


Figure 8. Differential intensity of CR electrons for PAMELA 2008 datasets. Points represent experimental data, the dashed line is the GALPROP LIS, and the solid line is the computed modulated spectrum. The bottom panel shows the relative difference between the numerical solution and experimental data.

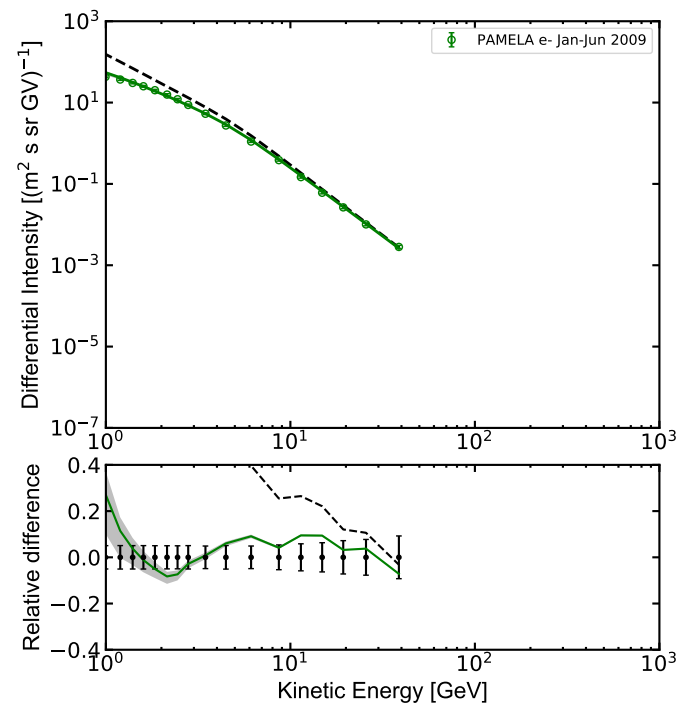


Figure 9. Differential intensity of CR electrons for PAMELA datasets integrated from January to June 2009. Points represent experimental data, the black dashed line is the GALPROP LIS, and the solid line is the computed modulated spectrum. The bottom panel shows the relative difference between the numerical solution and experimental data.

Table 4
Electron LIS

Kinetic energy, GeV	Differential intensity ^a	Kinetic energy, GeV	Differential intensity ^a	Kinetic energy, GeV	Differential intensity ^a	Kinetic energy, GeV	Differential intensity ^a
1.000e-03	3.481e+06	3.927e-02	3.225e+04	1.542e+00	6.057e+01	6.482e+01	5.236e-04
1.070e-03	3.710e+06	4.203e-02	2.935e+04	1.651e+00	5.145e+01	6.938e+01	4.167e-04
1.146e-03	3.523e+06	4.499e-02	2.671e+04	1.767e+00	4.370e+01	7.426e+01	3.318e-04
1.226e-03	3.288e+06	4.815e-02	2.431e+04	1.891e+00	3.713e+01	7.949e+01	2.644e-04
1.312e-03	3.056e+06	5.154e-02	2.212e+04	2.024e+00	3.155e+01	8.508e+01	2.108e-04
1.405e-03	2.835e+06	5.517e-02	2.014e+04	2.166e+00	2.681e+01	9.106e+01	1.681e-04
1.504e-03	2.627e+06	5.905e-02	1.834e+04	2.319e+00	2.278e+01	9.747e+01	1.342e-04
1.609e-03	2.431e+06	6.320e-02	1.670e+04	2.482e+00	1.935e+01	1.043e+02	1.071e-04
1.722e-03	2.246e+06	6.764e-02	1.521e+04	2.656e+00	1.642e+01	1.117e+02	8.560e-05
1.844e-03	2.074e+06	7.240e-02	1.386e+04	2.843e+00	1.392e+01	1.195e+02	6.841e-05
1.973e-03	1.912e+06	7.749e-02	1.262e+04	3.043e+00	1.179e+01	1.279e+02	5.470e-05
2.112e-03	1.761e+06	8.295e-02	1.149e+04	3.257e+00	9.962e+00	1.369e+02	4.374e-05
2.261e-03	1.621e+06	8.878e-02	1.046e+04	3.486e+00	8.397e+00	1.465e+02	3.499e-05
2.420e-03	1.490e+06	9.502e-02	9.525e+03	3.732e+00	7.054e+00	1.569e+02	2.800e-05
2.590e-03	1.368e+06	1.017e-01	8.669e+03	3.994e+00	5.904e+00	1.679e+02	2.240e-05
2.772e-03	1.256e+06	1.089e-01	7.887e+03	4.275e+00	4.919e+00	1.797e+02	1.793e-05
2.967e-03	1.151e+06	1.165e-01	7.173e+03	4.576e+00	4.076e+00	1.923e+02	1.435e-05
3.176e-03	1.055e+06	1.247e-01	6.521e+03	4.898e+00	3.358e+00	2.059e+02	1.149e-05
3.399e-03	9.658e+05	1.335e-01	5.926e+03	5.242e+00	2.748e+00	2.203e+02	9.193e-06
3.638e-03	8.835e+05	1.429e-01	5.382e+03	5.611e+00	2.235e+00	2.358e+02	7.358e-06
3.894e-03	8.077e+05	1.529e-01	4.886e+03	6.005e+00	1.806e+00	2.524e+02	5.889e-06
4.168e-03	7.380e+05	1.637e-01	4.433e+03	6.428e+00	1.451e+00	2.702e+02	4.713e-06
4.461e-03	6.739e+05	1.752e-01	4.019e+03	6.880e+00	1.160e+00	2.892e+02	3.772e-06
4.775e-03	6.150e+05	1.875e-01	3.640e+03	7.364e+00	9.239e-01	3.095e+02	3.018e-06
5.111e-03	5.609e+05	2.007e-01	3.295e+03	7.882e+00	7.335e-01	3.313e+02	2.415e-06
5.470e-03	5.114e+05	2.148e-01	2.979e+03	8.436e+00	5.811e-01	3.546e+02	1.932e-06
5.855e-03	4.660e+05	2.299e-01	2.690e+03	9.029e+00	4.598e-01	3.795e+02	1.545e-06
6.267e-03	4.244e+05	2.461e-01	2.426e+03	9.665e+00	3.634e-01	4.062e+02	1.236e-06
6.707e-03	3.864e+05	2.634e-01	2.185e+03	1.034e+01	2.871e-01	4.348e+02	9.887e-07
7.179e-03	3.517e+05	2.819e-01	1.964e+03	1.107e+01	2.268e-01	4.654e+02	7.907e-07
7.684e-03	3.200e+05	3.018e-01	1.762e+03	1.185e+01	1.791e-01	4.981e+02	6.323e-07
8.225e-03	2.910e+05	3.230e-01	1.577e+03	1.268e+01	1.415e-01	5.332e+02	5.056e-07
8.803e-03	2.646e+05	3.457e-01	1.409e+03	1.358e+01	1.118e-01	5.707e+02	4.042e-07
9.422e-03	2.406e+05	3.700e-01	1.255e+03	1.453e+01	8.829e-02	6.108e+02	3.231e-07
1.008e-02	2.186e+05	3.960e-01	1.115e+03	1.555e+01	6.976e-02	6.538e+02	2.583e-07
1.079e-02	1.987e+05	4.239e-01	9.886e+02	1.665e+01	5.512e-02	6.997e+02	2.064e-07
1.155e-02	1.805e+05	4.537e-01	8.739e+02	1.782e+01	4.356e-02	7.489e+02	1.650e-07
1.237e-02	1.640e+05	4.856e-01	7.703e+02	1.907e+01	3.444e-02	8.016e+02	1.318e-07
1.324e-02	1.489e+05	5.198e-01	6.771e+02	2.041e+01	2.722e-02	8.580e+02	1.053e-07
1.417e-02	1.353e+05	5.563e-01	5.934e+02	2.185e+01	2.152e-02	9.184e+02	8.416e-08
1.516e-02	1.229e+05	5.955e-01	5.185e+02	2.339e+01	1.703e-02	9.830e+02	6.724e-08
1.623e-02	1.116e+05	6.374e-01	4.517e+02	2.503e+01	1.347e-02	1.052e+03	5.372e-08
1.737e-02	1.014e+05	6.822e-01	3.923e+02	2.679e+01	1.066e-02	1.126e+03	4.291e-08
1.859e-02	9.206e+04	7.302e-01	3.398e+02	2.867e+01	8.439e-03	1.205e+03	3.427e-08
1.990e-02	8.363e+04	7.815e-01	2.934e+02	3.069e+01	6.680e-03	1.290e+03	2.737e-08
2.130e-02	7.597e+04	8.365e-01	2.527e+02	3.285e+01	5.304e-03	1.381e+03	2.186e-08
2.280e-02	6.903e+04	8.953e-01	2.171e+02	3.516e+01	4.192e-03	1.478e+03	1.746e-08
2.440e-02	6.273e+04	9.583e-01	1.861e+02	3.763e+01	3.316e-03	1.582e+03	1.394e-08
2.612e-02	5.701e+04	1.026e+00	1.592e+02	4.028e+01	2.633e-03	1.693e+03	1.113e-08
2.796e-02	5.182e+04	1.098e+00	1.359e+02	4.311e+01	2.077e-03	1.812e+03	8.888e-09
2.992e-02	4.712e+04	1.175e+00	1.158e+02	4.615e+01	1.649e-03	1.940e+03	7.096e-09
3.203e-02	4.285e+04	1.258e+00	9.861e+01	4.939e+01	1.310e-03	2.076e+03	5.665e-09
3.428e-02	3.897e+04	1.346e+00	8.387e+01	5.287e+01	1.042e-03	2.222e+03	4.522e-09
3.669e-02	3.545e+04	1.441e+00	7.129e+01	5.658e+01	8.282e-04	2.378e+03	3.610e-09

^a Differential intensity units: (m² s sr GV)⁻¹.